The inverse band-structure problem of finding an atomic configuration with given electronic properties

Alberto Franceschetti & Alex Zunger

National Renewable Energy Laboratory, Golden, Colorado 80401, USA

Modern crystal-growth techniques, such as molecular beam epitaxy or metal–organic chemical-vapour deposition, are capable of producing prescribed crystal structures, sometimes even in defiance of equilibrium, bulk thermodynamics. These techniques open up the possibility of exploring different atomic arrangements in search of a configuration that possesses given electronic and optical properties[1]. Unfortunately, the number of possible combinations is so vast, and the electronic properties are so sensitive to the details of the crystal structure, that simple trial-and-error methods (such as those used in combinatorial synthesis[2]) are unlikely to be successful. Here we describe a theoretical method that addresses the problem of finding the atomic configuration of a complex, multi-component system having a target electronic-structure property. As an example, we predict that the configuration of an $Al_{0.25}Ga_{0.75}As$ alloy having the largest optical bandgap is a $(GaAs)_2(AlAs)_1(GaAs)_4(AlAs)_1$ superlattice oriented in the [201] direction.

Conventional electronic-structure theory of solids, clusters and molecules proceeds by first specifying the spatial coordinates of all atomic species involved, and then calculating the ensuing energy levels and wavefunctions:

$$\text{Atomic configuration} \rightarrow \text{Electronic structure} \qquad (1)$$

We are interested in the counterpart to this direct approach: the 'inverse approach' of finding the atomic configuration that produces a prescribed electronic structure:

$$\text{Electronic structure} \rightarrow \text{Atomic configuration} \qquad (2)$$

In the context of optical properties, such a method would provide answers to questions like "For a given superlattice orientation, what is the layer sequence that has the maximum bandgap (or a pre-assigned bandgap, say 2 eV)?"[3]. In the context of transport properties, one could ask: "What is the crystal structure whose band structure maximizes Auger carrier multiplication?"[4]. Similar 'inverse problems' can be addressed in the context of vibrational and photonic properties, as well as for molecules and low-dimensional systems.

We describe here a solution to the 'inverse band-structure problem' based on a direct exploration of the space of atomic configurations in search of the configuration possessing given electronic properties. The formidable complexity of this problem is best illustrated by an example. Consider a pseudo-binary substitutional alloy $A_xB_{1-x}C$ of composition x, described by a unit cell of $2N$ lattice sites, such that each of the N cation sites is occupied by an A atom or a B atom. The number of possible atomic configurations is $N_{\text{config}} = N!/((xN)!(N - xN)!)$. For instance, for $x = 0.25$ and $2N = 128$, $N_{\text{config}} \approx 10^{14}$. Each configuration has, in principle, a different electronic structure, and therefore different electronic and optical properties. How many atomic configurations (N_{search}) is it necessary to explore in order to find the configuration that has the target electronic properties? Clearly, if this approach is to be successful N_{search} should be small compared to N_{config}. We search the configuration space using a simulated-annealing algorithm that is able to 'learn the system' relatively quickly ($N_{\text{search}} \approx 10^4$) by retaining only those configurations that are conducive to the target electronic structure. Coupled with a fast, "Order N" solution of the Schrödinger equation, this method allows us to determine the target configuration of systems containing a few hundred atoms.

We consider substitutional systems described by an underlying lattice structure of N sites. An atomic configuration σ is defined as a set of N 'occupation variables' $\{S_1, S_2, \cdots S_N\}$, where S_i denotes the identity of the atom located at lattice site i. The configuration variables $\{S_i\}$ can be restricted to describe a particular experimental growth sequence, for example an $A_pB_qA_rB_s$ … superlattice (where p, q, r, s denote the number of monolayers) oriented in the [001] direction. We then consider a set of electronic-structure properties $P_\alpha(\sigma)$, defined for every configuration σ, and the corresponding target properties P_α^{target}. The subscript α identifies specific properties, such as bandgaps, effective masses or oscillator strengths. The N-variable object function

$$O(\sigma) = \sum_\alpha \omega_\alpha |P_\alpha(\sigma) - P_\alpha^{\text{target}}|, \qquad (3)$$

where ω_α is the weight assigned to the property P_α, describes the 'distance' between the electronic structure of the configuration σ and the target electronic structure. This function $O(\sigma)$ is minimized by varying the configuration variables $\sigma = \{S_1, S_2, \ldots S_N\}$, and calculating at each step $P_\alpha(\sigma)$ from electronic-structure theory. This approach requires a fast-learning method of sampling the configuration space, and a numerically efficient yet physically accurate method of calculating the electronic structure of a given atomic configuration. Here we describe these methods.

(1) *Exploration of the configuration space.* The simulated-annealing technique is an efficient algorithm for finding the global minimum of a multi-variable, multi-valley function. Given an atomic configuration σ, a trial configuration σ_{trial} is generated by elementary Monte Carlo moves, such as changing the identity of one atom, or swapping the positions of two atoms of different types. The trial configuration σ_{trial} is accepted with a probability distribution

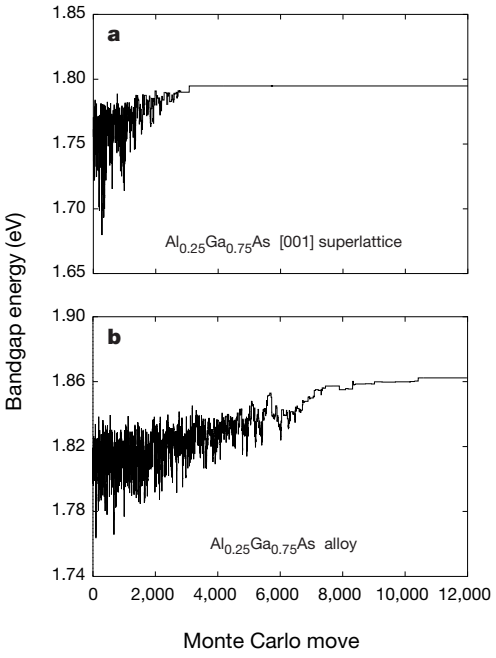

Figure 1 Simulated-annealing search of the maximum-gap configuration. The bandgap is shown as a function of the number of elementary Monte Carlo moves. The simulation cell includes 64 atoms for superlattices oriented in the [001] direction and 128 atoms for alloys. **a**, [001] $Al_{0.25}Ga_{0.75}As$ superlattices; **b**, $Al_{0.25}Ga_{0.75}As$ alloys.

Table 1 Maximum-gap configurations of $Al_xGa_{1-x}As$ and $Ga_xIn_{1-x}P$ superlattices oriented in the [001] direction

Concentration x	$Al_xGa_{1-x}As$	$Ga_xIn_{1-x}P$
0.250	$(AlAs)_1\,(GaAs)_3$	$(GaP)_1\,(InP)_3$
0.333	$(AlAs)_1\,(GaAs)_2$	$(GaP)_1\,(InP)_2$
0.500	$(AlAs)_2\,(GaAs)_2$	$(GaP)_1\,(InP)_1$
0.666	$(AlAs)_2\,(GaAs)_1$	$(GaP)_2\,(InP)_1$
0.750	$(AlAs)_3\,(GaAs)_1$	$(GaP)_3\,(InP)_1$

$p(\Delta O) = \min[1, \exp(-\Delta O/T)]$ where $\Delta O = O(\sigma_{trial}) - O(\sigma)$ and T is a fictitious temperature parameter. By slowly decreasing the temperature to zero, the system is allowed to settle into the configuration that minimizes the object function O. We use an exponential temperature profile $T_n = T_0\exp(-n/\tau)$, where T_0 is the initial temperature and τ is the temperature decay rate. Here n is the index of the simulated-annealing steps; each simulated-annealing step includes several elementary moves. The exponential temperature profile allows us to reduce the acceptance ratio in a nearly linear fashion. If the annealing process is too fast the system can become trapped in a local-minimum configuration. We can detect and avoid local minima by changing the initial configuration and/or the temperature profile.

(2) *Electronic structure of a given atomic configuration.* This is done in three steps:

First, atomic relaxations: For each elementary Monte Carlo move the system is relaxed into the local energy minimum corresponding to the selected configuration (that is, without interchange of atoms). This task is accomplished using a valence-force-field method[5] whose parameters are fitted to *ab initio* total-energy calculations for various configurations. The outputs are the equilibrium atomic positions $\{\mathbf{R}_n, n = 1\ldots N_{at}\}$ of the selected configuration.

Second, realistic hamiltonian: it is well known[6] that the conventional first-principle description of optical properties—the local-density approximation (LDA) to density-functional theory—produces systematic errors in the bandgap, a quantity that we are interested in here. We thus do not use the LDA approach. Instead, the electronic structure of each configuration is described by a semi-empirical pseudopotential hamiltonian:

$$\hat{H} = -\frac{\hbar^2}{2m}\nabla^2 + \sum_{n=1}^{N_{at}} v_n(\mathbf{r} - \mathbf{R}_n) \qquad (4)$$

where m is the bare electron mass. The total pseudopotential is given by a linear superposition of local atomic pseudopotentials $v_n(\mathbf{r} - \mathbf{R}_n)$ centred at the atomic positions $\{\mathbf{R}_n, n = 1\ldots N_{at}\}$. Unlike conventional empirical pseudopotentials[7], the atomic pseudopotentials v_n are fitted[8] not only to observed bulk interband transition energies, but also to (1) effective masses, deformation potentials, and band offsets, and (2) bulk single-particle wavefunctions calculated using density-functional theory in the local-density approximation. Since we are dealing here with bulk-like atomic configurations that are free from defects or surfaces (each cation is coordinated by anions and each anion is coordinated by cations), the hamiltonian of equation (4) should provide an accurate description of all the configurations reached by the Monte Carlo sampling. Such modern semi-empirical pseudopotentials have successfully described the electronic and optical properties of substitutional systems, such as semiconductor alloys and superlattices[9,10].

Third, fast diagonalization: Since we are interested in electronic properties that involve band-edge energy levels and wavefunctions, the hamiltonian of equation (4) is diagonalized using a computationally efficient method that focuses on an energy window around the bandgap[11]. In this approach, the band-edge energies ϵ_i and wavefunctions ψ_i are obtained by solving the 'folded-spectrum' equation:

$$[\hat{H} - \epsilon_{ref}]^2\psi_i(\mathbf{r}) = (\epsilon_i - \epsilon_{ref})^2\psi_i(\mathbf{r}), \qquad (5)$$

where ϵ_{ref} is an arbitrary reference energy. The 'ground state' of equation (5) coincides with the eigenstate of the hamiltonian in equation (4) whose energy is closest to the reference energy ϵ_{ref}. Therefore, by choosing the reference energy in the bandgap, the band edge states can be readily obtained by minimizing the functional $A[\psi] = \langle\psi|(\hat{H} - \epsilon_{ref})^2|\psi\rangle$. For each Monte Carlo move, the wavefunctions of the last accepted configuration are used as initial guesses for the iterative solution of equation (5).

We consider here AlAs/GaAs and GaP/InP substitutional systems. The underlying lattice has the zinc-blende structure, with cation atoms occupying one of the two interpenetrating f.c.c. sublattices and anion atoms occupying the other f.c.c. sublattice. The AlAs/GaAs system has a small lattice mismatch, so we assume that, for every configuration, the atoms occupy their ideal (zinc-blende) positions. The GaP/InP system, on the other hand, has a substantial lattice mismatch (~7%). Thus, for each configuration the atoms (both cations and anions) are allowed to relax into their local equilibrium positions. Note that the $Al_xGa_{1-x}As$ and $Ga_xIn_{1-x}P$ random alloys are characterized by a crossover from a direct-gap semiconductor (with both the valence-band maximum and the conduction-band minimum located at the Γ point of the Brillouin zone) to an indirect-gap semiconductor (with the valence-band maximum at the Γ point and the conduction-band minimum near the X point) as a function of the concentration x. Our approach is capable of addressing substitutional systems that display such types of electronic phase transition.

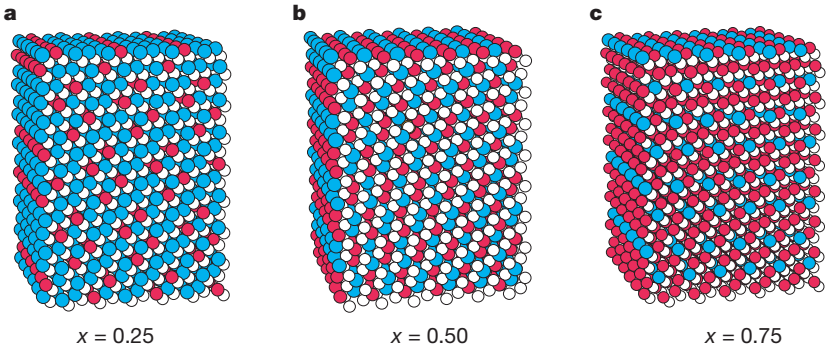

Figure 2 Maximum-gap configurations of $Al_xGa_{1-x}As$ alloys for different Al concentrations x. Ga atoms are denoted by blue circles, Al atoms by red circles, and As atoms by white circles. **a**, For $x = 0.25$ the maximum-gap configuration corresponds to a $(GaAs)_2(AlAs)_1(GaAs)_4(AlAs)_1$ superlattice in the [201] orientation, and the bandgap is 1.86 eV. **b**, For $x = 0.50$ the maximum-gap configuration is a $(GaAs)_2(AlAs)_2$ superlattice in the [201] direction (chalcopyrite structure), and the bandgap is 2.12 eV. **c**, For $x = 0.75$ the maximum-gap configuration is a $(GaAs)_1(AlAs)_3$ superlattice in the [201] orientation (famatinite structure), and the bandgap is 2.18 eV.

The first 'inverse problem' we consider is finding the configuration of $Al_xGa_{1-x}As$ and $Ga_xIn_{1-x}P$ alloys and superlattices that maximizes the optical bandgap at a given concentration x. Interestingly, the complementary "minimum-gap problem" has a trivial solution for these systems (but not in general, see for example ref. 12), as the configuration that minimizes the bandgap corresponds to the phase-separated alloy for any concentration x. The simulation cell includes 64 atoms for superlattices oriented in the [001] direction and 128 atoms for alloys. While these unit cells may be too small to describe the electronic structure of disordered superlattices or random alloys, we expect that the maximum-gap configuration will be attained by an ordered structure with a relatively small unit cell. Thus, we believe that the structures that maximize the bandgap are fully described by the present simulation cells.

Figure 1 shows representative simulation profiles of the bandgap as a function of the number of elementary Monte Carlo moves. We see that only a few thousand moves are required to reach the configuration having the maximum bandgap ($N_{search} < 10{,}000$). This should be compared with the number of possible configurations, which is of the order of $N_{config} \approx 10^7$ for the 64-atom cell of Fig. 1a and $N_{config} \approx 10^{14}$ for the 128-atom cell of Fig. 1b. The number of Monte Carlo moves increases superlinearly with the number of atoms in the simulation cell. However, it increases at a much slower rate than the number of configurations.

The maximum-gap configurations of $Al_xGa_{1-x}As$ and $Ga_xIn_{1-x}P$ superlattices in the [001] direction are summarized in Table 1. They correspond to the shortest-period superlattices compatible with the assigned cation concentration, with one exception: the $(GaAs)_1(AlAs)_1$ superlattice has a smaller bandgap than the $(GaAs)_2(AlAs)_2$ superlattice, because the folding of the X point of the Brillouin zone into the Γ point causes a strong coupling between the Γ_{1c} and X_{3c} alloy states, pushing the energy of the Γ_{1c}-derived conduction-band minimum of the 1×1 superlattice down.

The maximum-gap configurations of $Al_xGa_{1-x}As$ alloys with different Al concentrations x are shown in Fig. 2. We find that the maximum-gap configuration of the $Al_{0.25}Ga_{0.75}As$ alloy (Fig. 2a) corresponds to a $(GaAs)_2(AlAs)_1(GaAs)_4(AlAs)_1$ superlattice in the [201] orientation. Previous "cluster expansion" models[3] (describing the bandgap of an arbitrary configuration by a linear combination of energies associated with characteristic "figures", such as pairs or triangles) carried out in the LDA framework had shown that this configuration has the largest bandgap among $Al_{0.25}Ga_{0.75}As$ alloys. However, the value of the bandgap in ref. 3 was affected by the LDA error. For $x = 0.50$ the maximum-gap configuration (Fig. 2b) is a $(GaAs)_2(AlAs)_2$ superlattice in the [201] orientation (chalcopyrite structure). Finally, for $x = 0.75$ the maximum-gap configuration (Fig. 2c) is a $(GaAs)_1(AlAs)_3$ superlattice in the [201] direction (famatinite structure). All the maximum-gap configurations of AlGaAs alloys are predicted to be superlattices in the [201] direction. This result can be understood in terms of folding relationships. For [201] superlattices the X and W points of the bulk Brillouin zone are folded into the Γ point of the superlattice Brillouin zone. However, the X- and W-derived states are weakly coupled to the Γ-derived band-edge states. As a result, [201] superlattices are not affected by the band-gap reduction characteristic of other superlattice orientations. Note that while the $(GaAs)_2(AlAs)_1$ $(GaAs)_4(AlAs)_1$ structure has a direct bandgap (large oscillator strength), the chalcopyrite and famatinite structures have an indirect bandgap (small oscillator strength).

As a second example, we have calculated the configurations of AlAs/GaAs and GaP/InP superlattices in the [001] orientation having a pre-assigned bandgap (1.8 eV for AlAs/GaAs superlattices and 1.9 eV for GaP/Inp superlattices) and the largest possible oscillator strength. In these simulations the concentration x is allowed to change; the lattice constant, however, is kept fixed at the average value of the lattice constants of the binary constituents.

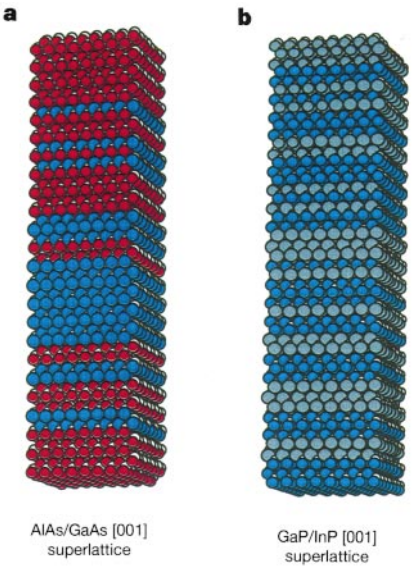

Figure 3 Atomic configurations of superlattices in the [001] orientation having a pre-assigned bandgap and maximum bandgap oscillator strength. The target bandgap is 1.8 eV for AlAs/GaAs superlattices and 1.9 eV for GaP/InP superlattices. Ga atoms are denoted by blue circles, Al atoms by red circles, In atoms by grey circles, and As and P atoms by white circles. **a**, AlAs/GaAs superlattice; **b**, GaP/InP superlattice.

The prescribed bandgap is achieved within a few milli-electronvolts. The atomic configurations having the target electronic properties are shown in Fig. 3. In the case of AlAs/GaAs (Fig. 3a), the 'core' of the resulting configuration is a $(GaAs)_2(AlAs)_2(GaAs)_9(AlAs)_2$ $(GaAs)_2$ quantum well embedded in AlAs. The additional Ga layers in the structure do not affect the electronic properties significantly. In the case of GaP/InP (Fig. 3b), the resulting configuration is a superlattice with layer thicknesses ranging from one to three layers.

It is interesting to speculate whether the structures identified via an intensive computer search could have been anticipated based on analytical exploration or physical insight. We suspect that although in some simple cases, such as the short-period superlattices of Table 1, one can rationalize the results after the fact in terms of band-folding relationships, in general the non-intuitive relation between the reciprocal-space band structure and the real-space atomic configuration (equation (2)) makes *a priori* guesses unlikely. In fact, some of the structures we predict are unsuspected on the basis of the normal insights underlying band theory.

Finally, we have applied our method to semiconductor alloys and superlattices, but the same algorithm could be applied to the optimization of the electronic structure of complex molecules and clusters. □

Received 3 May; accepted 20 September 1999.

1. Capasso, F. *Physics of Quantum Electron Devices* (Springer, Berlin, 1990).
2. Wilson, S. R. & Czarnik, A. W. *Combinatorial Chemistry: Synthesis and Application* (Wiley, New York, 1997).
3. Magri, R. & Zunger, A. Real-space description of semiconducting band gaps in substitutional systems. *Phys. Rev. B* **44,** 8672–8684 (1991).
4. Werner, J. H., Kolodinski, S. & Queisser, H. J. Novel optimization principles and efficiency limits for semiconductor solar cells. *Phys. Rev. Lett.* **72,** 3851–3854 (1994).
5. Silverman, A., Zunger, A., Kalish, R. & Adler, J. Atomic-scale structure of disordered $Ga_{1-x}In_xP$ alloys. *Phys. Rev. B* **51,** 10795–10816 (1995).
6. Zunger, A. & Freeman, A. J. Ground- and excited-state properties of LiF in the local-density formalism. *Phys. Rev. B* **16,** 2901–2926 (1977).
7. Chelikowsky, J. R. & Cohen, M. L. Nonlocal pseudopotential calculations for the electronic structure of eleven diamond and zinc-blende semiconductors. *Phys. Rev. B* **14,** 556–582 (1976).
8. Wang, L. W. & Zunger, A. Local-density-derived semiempirical pseudopotentials. *Phys. Rev. B* **51,** 17398–17416 (1995).
9. Mader, K., Wang, L. W. & Zunger, A. Electronic structure of intentionally disordered AlAs/GaAs superlattices. *Phys. Rev. Lett.* **74,** 2555–2558 (1995).

10. Mattila, T., Wei, S.-H. & Zunger, A. Electronic structure of "sequence mutations" in ordered $GaInP_2$ alloys. *Phys. Rev. Lett.* **83,** 2010–2013 (1999).
11. Wang, L. W. & Zunger, A. Solving Schrödinger's equation around a desired energy: Application to silicon quantum dots. *J. Chem. Phys.* **100,** 2394–2397 (1994).
12. Bellaiche, L., Wei, S. H. & Zunger, A. Localization and percolation in semiconductor alloys: GaAsN vs. GaAsP. *Phys. Rev. B* **54,** 17568–17576 (1996).

Acknowledgements

This work was supported by the US Department of Energy, Office of Science, Division of Materials Science.

Correspondence and requests for materials should be addressed to A.F. (e-mail: afrances@nrel.gov).

Frozen-bed Fennoscandian and Laurentide ice sheets during the Last Glacial Maximum

Johan Kleman* & Clas Hättestrand*

Department of Physical Geography, Stockholm University, S-106 91 Stockholm, Sweden
** The authors contributed equally to this work*

The areal extents of the Laurentide and Fennoscandian ice sheets during the Last Glacial Maximum (about 20,000 years ago) are well known[1], but thickness estimates range widely, from high-domed[2] to thin[3], with large implications for our reconstruction of the climate system regarding, for example, Northern Hemisphere atmospheric circulation and global sea levels. This uncertainty stems from difficulties in determining the basal temperatures of the ice sheets and the shear strength of subglacial materials[4], a knowledge of which would better constrain reconstructions of ice-sheet thickness. Here we show that, in the absence of direct data, the occurrence of ribbed moraines in modern landscapes can be used to determine the former spatial distribution of frozen- and thawed-bed conditions. We argue that ribbed moraines were formed by brittle fracture of subglacial sediments, induced by the excessive stress at the boundary between frozen- and thawed-bed conditions resulting from the across-boundary difference in basal ice velocity. Maps of glacial landforms from aerial photographs of Canada and Scandinavia reveal a concentration of ribbed moraines around the ice-sheet retreat centres of Quebec, Keewatin, Newfoundland and west-central Fennoscandia. Together with the evidence from relict landscapes that mark glacial areas with frozen-bed conditions, the distribution of ribbed moraines on both continents suggest that a large area of the Laurentide and Fennoscandian ice sheets was frozen-based—and therefore high-domed and stable—during the Last Glacial Maximum.

The glaciological factors controlling the location of thermal zones (surface temperature, ice thickness, geothermal flux, strain heating) under ice sheets are well understood[5], but because of the absence of direct subglacial palaeotemperature records, the actual basal thermal conditions under the Fennoscandian ice sheet (FIS) and Laurentide ice sheet (LIS) have remained elusive. Wide zones of subglacial till (glacially transported sediments) deformation have been invoked in modelling experiments predicting low ice-sheet profiles[3], but without data on the phase state (frozen or thawed) of the sediments in deformable bed areas under glacial conditions, the validity of these models has been difficult to verify. The problem is that the rheology of subglacial till is extremely sensitive to the phase state of the interstitial water; frozen subglacial till is much stronger than ice, whereas thawed till under high water pressures can be deformed by overriding ice[6]. We focus here on the landform record interpreted to result from the phase-state control on soil strength (and thereby landform-building processes) and perform an inversion of the record: that is, we use the spatial distribution of diagnostic landforms to gain insight into the former subglacial phase- and temperature-regime under the FIS and LIS.

The two main subglacial landform groups resulting from reshaping of subglacial sediments are: (1) drumlins and flutings (flow-parallel streamlined till ridges, 0.1–20 km in length), created by particle-by-particle entrainment and lodgement processes or plastic deformation of till masses[7], and (2) ribbed moraines or Rogen moraines (fields of till ridges, 0.1–1 km in length, formed transverse to ice flow), with a debated mode of formation[8]. Drumlins and flutings cover 90% of the terrestrial parts of the LIS[9,10] and FIS areas, but ribbed moraines less than 10%, with a spatial distribution that is extremely selective when compared to the lineation distribution. There is a third important group of subglacial landscapes: those which have been left essentially unmodified by the last ice sheet due to sustained frozen-bed conditions and absence of basal sliding[11].

Previous formation hypotheses for ribbed moraine suggested compressive flow (caused by topography, that is, by bedrock depressions)[12], or the type and amount of basal debris load[13] as the primary controls on its formation. As hilly topography and coarse-grained tills are widespread in areas of Precambrian basement rocks (shown yellow in Fig. 1a and b), these hypotheses imply that ribbed moraines would occur geographically dispersed, wherever local topographic or substratum conditions were favourable. The concentration of ribbed moraines in the four retreat centres of Quebec, Keewatin, Newfoundland and west-central Fennoscandia (Fig. 1a and b), and their absence in other areas of hilly relief and coarse-grained tills, indicates that some other type of primary control on their distribution exists.

Ribbed moraines are conspicuously lacking in the southern parts of both ice-sheet areas where thawed-bed conditions prevailed after the Last Glacial Maximum (LGM), and it thus appears unlikely that ribbed moraine formed under completely thawed-bed conditions. The concentric arrangement of ribbed moraines around late-glacial retreat centres, and their affinity to frozen-bed areas, indicates that the primary control is a time-dependent basal thermal evolution. The stratigraphical and structural composition of ribbed moraine is highly variable (from laminated silt to shattered bedrock), and generally follows local variations in the till composition[8,14]. Hence, ribbed moraines cannot be linked to any specific depositional facies. Rather, the deposition of the sediments in ribbed moraine ridges appears to be genetically unrelated to the actual landform-shaping process[8,15], predating it. Morphological evidence (Fig. 2a; detailed till block outline matching, grating patterns, strike-slip faulting of till slabs, rotation of discrete till blocks) indicate that individual ridges were once part of a coherent drift sheet, and we thus infer that formation of ribbed moraine occurred by brittle fracture of drift sheets. Such brittle behaviour cannot occur in unfrozen drift (due to its low cohesive strength), and we therefore argue for a primary thermal control on ribbed moraine formation, by fracturing of frozen drift sheets during the transition from frozen to thawed conditions in an extensional basal regime (Fig. 3). Extreme stress concentrations develop at frozen–thawed boundaries[16], because of the abrupt increase in basal ice flow velocity, and we infer brittle fracture of drift sheets to have occurred at migrating frozen–thawed boundaries. The often observed lack of material between ribbed moraine ridges[15] is not compatible with alternative formation processes of glaciotectonic stacking and sediment thickening[12]. The typical 150–600 m spacing of individual ribbed moraine ridges contrasts sharply with the observed tightly folded "wrinkled-carpet" morphology of subglacial compressional ridges[17].

Relict landscapes are defined by ground surfaces and landforms essentially unmodified during overriding by the last ice sheet[18] (Fig. 2b and c). In these landscapes glacial meltwater traces from the last deglaciation (that is, meltwater channels and ice dammed